Check for updates

View Article Online
View Journal

EES Solar

Accepted Manuscript

This article can be cited before page numbers have been issued, to do this please use: A. Singha, T. Zhang, A. Paul, M. M. Anas, K. Raitani, M. Misra, S. Manna, V. Kumar, S. Mallick, K. R. Balasubramaniam, P. Nair, F. Gao and D. Kabra, *EES Sol.*, 2026, DOI: 10.1039/D5EL00175G.

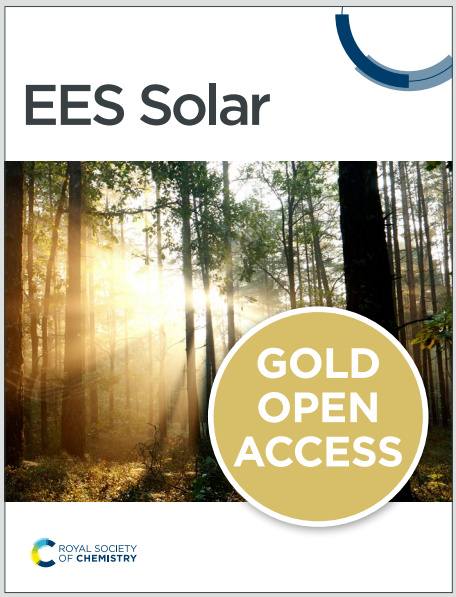

This is an Accepted Manuscript, which has been through the Royal Society of Chemistry peer review process and has been accepted for publication.

Accepted Manuscripts are published online shortly after acceptance, before technical editing, formatting and proof reading. Using this free service, authors can make their results available to the community, in citable form, before we publish the edited article. We will replace this Accepted Manuscript with the edited and formatted Advance Article as soon as it is available.

You can find more information about Accepted Manuscripts in the Information for Authors.

Please note that technical editing may introduce minor changes to the text and/or graphics, which may alter content. The journal's standard Terms & Conditions and the Ethical guidelines still apply. In no event shall the Royal Society of Chemistry be held responsible for any errors or omissions in this Accepted Manuscript or any consequences arising from the use of any information it contains.

ROYAL SOCIETY
OF CHEMISTRY

View Article Online
DOI: 10.1039/D5EL00175G

Broader Context:

Silicon/perovskite tandem solar cells represent an emerging pathway toward next-generation photovoltaics, yet interfacial defects and energy level mismatches between perovskite absorbers and charge transport layers (CTLs) critically limit their efficiency and stability. Conventional LiTFSI- and t-BP-doped Spiro-MeOTAD hole transport layers (HTLs) require post-oxidation and exhibit poor ionic and environmental stability. Here, an ion-modulated, post-oxidation-free Spiro-MeOTAD employing 4-tert-butyl-1-methylpyridinium bis(trifluoromethanesulfonyl)imide ($TBMP^+TFSI^-$) is introduced to achieve controlled work function tuning and effective interfacial defect passivation. This strategy suppresses non-radiative recombination, enhances quasi-Fermi level splitting, and improves V_{OC} and fill factor across diverse perovskite band gaps. Integration of the optimized transparent perovskite subcells with an *n*-TOPCon Si bottom cell in a 4-terminal configuration delivers a power conversion efficiency of 30.2%. These findings establish ion-modulated Spiro-MeOTAD as a robust, scalable HTL design for high-efficiency and durable perovskite/silicon tandem photovoltaics.

Open Access Article. Published on 09 January 2026. Downloaded on 1/22/2026 5:00:21 AM.
This article is licensed under a Creative Commons Attribution-NonCommercial 3.0 Unported Licence.

EES Solar Accepted Manuscript

View Article Online
DOI: 10.1039/D5EL00175G

Bandgap Tunable Transparent Perovskite Solar Cells for 4T Si/perovskite Tandem Photovoltaics with PCE > 30% via Rational Interface Management

Abhijit Singha,[1†] Tiankai Zhang,[2†] Ananta Paul,[3] M. M. Anas,[4] Karthik Raitani,[5] Manas Misra,[5] Subir Manna,[5] Vishnu Kumar,[5] Sudhanshu Mallick,[3] K. R. Balasubramaniam,[1] Pradeep R. Nair,[4*] Feng Gao,[2*] Dinesh Kabra[5*]

† Contributed equally to this work.

[1]Department of Energy Science and Engineering, Indian Institute of Technology Bombay, Mumbai, 400076, India

[2]Department of Physics, Chemistry and Biology (IFM), Linkoping University, Linkoping, 58183, Sweden

[3]Department of Metallurgical Engineering and Material Science, Indian Institute of Technology Bombay, Mumbai, 400076, India

[4]Department of Electrical Engineering, Indian Institute of Technology Bombay, Powai, Mumbai 400076,India.

[5]Department of Physics, Indian Institute of Technology Bombay, Powai, Mumbai 400076, India.

*Corresponding authors – prnair@ee.iitb.ac.in, feng.gao@liu.se, dkabra@iitb.ac.in

Open Access Article. Published on 09 January 2026. Downloaded on 1/22/2026 5:00:21 AM.
This article is licensed under a Creative Commons Attribution-NonCommercial 3.0 Unported Licence.

EES Solar Accepted Manuscript

Abstract

View Article Online
DOI: 10.1039/D5EL00175G

Open Access Article. Published on 09 January 2026. Downloaded on 1/22/2026 5:00:21 AM.
This article is licensed under a Creative Commons Attribution-NonCommercial 3.0 Unported Licence.

Silicon/perovskite tandem solar cells are predominantly recognized as a promising next-generation photovoltaic technology. The precise control of interfacial defects with appropriate energy level alignment between charge transport layers (CTLs) and the perovskite absorber is a crucial factor influencing the overall photovoltaic performance of perovskite solar cells (PSCs). This study investigates the substitution of conventional Lithium *bis*(trifluoromethane)sulfonimide (LiTFSI)- and 4-*tert*-butylpyridine (t-BP)-doped Spiro-MeOTAD with a post-oxidation-free, ion-modulated Spiro-MeOTAD hole transport layer (HTL) for tunable bandgap transparent PSCs. The incorporation of 4-*tert*-butyl-1-methylpyridinium *bis*(trifluoromethanesulfonyl)imide ($TBMP^{+}TFSI^{-}$) enables reduced Shockley-Read Hall (SRH) recombination with controlled work function tuning, leading to enhanced quasi-Fermi level splitting (QFLS). Three different perovskite compositions are employed, with perovskite 2 (1.61 eV) demonstrating optimal performance with both control and ion-modulated Spiro-MeOTAD, resulting in minimal photovoltaic performance deviations. In contrast, perovskite 1 (1.52 eV) and perovskite 3 (1.72 eV) exhibit suboptimal opto-electronic properties with the control HTL. The $TBMP^{+}TFSI^{-}$-doped Spiro-MeOTAD HTL enhances photoluminescence quantum efficiency and carrier lifetime by reducing interfacial defects, improving V_{OC}, and fill factor (FF) in agreement with our detailed simulation results. Integrating the optimized PSCs with an *n*-type tunnel oxide passivated contact (*n*-TOPCon) silicon (Si) solar cell in a 4-terminal (4T) tandem configuration achieves a power conversion efficiency (PCE) of 30.2%, highlighting the potential of ion-modulated Spiro-MeOTAD for efficient and stable tandem solar cells.

Keywords

Spiro-MeOTAD, Ageing-free Spiro-MeOTAD, Hole transport layer, Transparent perovskite solar cells, Si/perovskite tandem solar cells

EES Solar Accepted Manuscript

Introduction

View Article Online
DOI: 10.1039/D5EL00175G

Open Access Article. Published on 09 January 2026. Downloaded on 1/22/2026 5:00:21 AM.
This article is licensed under a Creative Commons Attribution-NonCommercial 3.0 Unported Licence.

EES Solar Accepted Manuscript

The discovery of hybrid organic and inorganic lead halide perovskites as a photo-absorber material has ushered in a ground-breaking era in photovoltaics (PV) technology. It exhibits exceptional optoelectronic properties, enabling near-theoretical power conversion efficiency (PCE) projection while significantly reducing fabrication costs compared to conventional monocrystalline silicon (Si) photovoltaics.[1–6] Moreover, beyond standalone applications, perovskites have also facilitated the development of tandem or multijunction solar cells. This offers a pathway to surpass the efficiency limits of single-junction devices, particularly for terrestrial applications, owing to their advantageous photovoltaic properties and exceptional bandgap tunability.[7–12] The facile and efficient tunability of the bandgap, combined with their superior light absorption characteristics, makes perovskite solar cells (PSCs) highly suitable for integration into tandem configurations, enabling higher PCEs than single-junction solar cells.[13–15] Notably, the achievement of 32.5% and 33.7% efficiency in two-terminal (2T) Si/perovskite tandem solar cells by academic institutions, along with a 34.9% efficiency reported by industrial laboratories, underscores the transformative potential of this technology for the commercialization of tandem solar cells in terrestrial applications.[13,16–19] Even though the Si/perovskite 2T tandem solar cells represent a promising and transformative advancement in PV technology. However, a significant challenge hindering their commercialization is the considerable disparity in operational lifetimes between Si and perovskite sub-cells. In this context, four-terminal (4T) tandem solar cells offer a commercially viable alternative by providing greater flexibility.[20,21] Specifically, in the event of perovskite sub-cell degradation, replacement is feasible without compromising the overall operational lifespan of the tandem configuration, thereby enhancing long-term stability and reliability at a fraction of the overall levelized cost of electricity (LCOE).[22,23]

Bandgap-tunable PSCs are essential components of tandem solar cells, where perovskite offers exceptional bandgap tunability with outstanding efficiency. However, a key observation in these solar cells is that an increase in bandgap is accompanied by a roughly linear decline in current density. But, the expected improvement in open-circuit voltage (V_{OC}) does not scale proportionally, leading to a reduction in the overall PCE.[24] This discrepancy arises from an increase in defect densities at higher bandgap perovskites as well as the shifted energy levels, which jointly lower the PV performance by introducing additional non-radiative recombination pathways.[25] Transparent PSCs are essential for the development of tandem solar cells, as they enable efficient light transmission to the bottom sub-cell.[26] In these devices, the conventional opaque metal electrode is replaced with a transparent electrode, allowing photons beyond the

View Article Online
DOI: 10.1039/D5EL00175G

Open Access Article. Published on 09 January 2026. Downloaded on 1/22/2026 5:00:21 AM.
This article is licensed under a Creative Commons Attribution-NonCommercial 3.0 Unported Licence.

EES Solar Accepted Manuscript

perovskite band edge to be utilized by the underlying absorber.[27] Transparent PSCs are typically fabricated in either a negative-intrinsic-positive (*n-i-p*) or positive-intrinsic-negative (*p-i-n*) configuration. While the *p-i-n* architecture is the preferred choice for 2T Si/perovskite tandem solar cells due to reduced parasitic absorption in charge transport layers (CTLs), particularly since incident light enters from the thinner electron transport layer (ETL) side, its counterpart, the *n-i-p* structure, is better suited for 4T tandem configurations.[28] The *n-i-p* design benefits from the use of stable inorganic ETLs and mitigates the parasitic absorption losses associated with the commonly used spiro-MeOTAD hole transport layer (HTL), as light enters from the ETL/perovskite interface.[29] Moreover, a given set of traditional CTLs is typically optimized for a specific perovskite bandgap value. Any variation in the perovskite bandgap can lead to energy level misalignment at the CTL/perovskite interface, particularly at the HTL/perovskite interface.[30] This misalignment is more pronounced at the HTL junction, as the valence band of the perovskite is predominantly influenced by halide orbitals, making it highly sensitive to changes in halide composition.[31,32] This misalignment induces band offsets, thereby lowering the implied open circuit voltage (iV_{OC}) and ultimately reducing device efficiency.[30] To address these challenges, researchers have investigated various strategies, including (i) the incorporation of interfacial layers between CTLs and the perovskite absorber to mitigate band misalignment, (ii) the selection of CTLs with appropriate band alignment, and (iii) bulk perovskite modulation to achieve efficient band alignment. For instance, Caprioglio et al. systematically quantified the impact of misaligned CTLs on the V_{OC} and overall device efficiency. Their study demonstrated that integrating low-dimensional perovskites as interfacial passivation layers effectively reduces the band offset, thereby enhancing V_{OC}, particularly in wide-bandgap (1.8 eV) perovskite absorbers.[25] Furthermore, Wang et al. incorporated alkylammonium bromide-based interfacial layers with varying chain lengths to form a 2D/3D heterostructure, achieving a maximum V_{OC} of 1.31 V in a triple-cation mixed-halide perovskite with a bandgap of 1.72 eV.[33] Additionally, Jaysankar et al. demonstrated that the incorporation of an atomic layer deposition (ALD)-derived Al_2O_3 passivation layer reduced the V_{OC} deficit, resulting in a 27.1% efficient 4-terminal (4T) Si/perovskite tandem solar cell.[34]

Beyond these approaches, several studies have also focused on modifying or incorporating different HTLs to mitigate V_{OC} loss. For example, Zhao et al. employed phosphorus-modulated NiO as an HTL in *p-i-n* PSCs, achieving a mere 24.69 % relative V_{OC} loss and developing an all-perovskite, 2T monolithic tandem solar cell with a PCE of 27.66 %.[35] Similarly, Wei et al. demonstrated that the incorporation of a bromine-substituted self-assembled monolayer

View Article Online
DOI: 10.1039/D5EL00175G

(SAM)-based HTL enabled the device to reach 90 % of the Shockley–Queisser (S-Q) V_{oc} limit for a 1.79 eV bandgap perovskite.[36] In addition to interfacial engineering, bulk perovskite modulation has also been investigated as a strategy to enhance V_{OC}. For example, Zhao et al. reported that the incorporation of phenethyl ammonium chloride (PMACl) resulted in lowering the V_{OC} deficit to 0.418 V.[37] Collectively, these studies underscore the importance of optimizing band alignment in bandgap-tunable PSCs to minimize V_{OC} deficits and ultimately achieve higher PCEs.

The inherent instability of PSCs is hindering their commercial field deployment.[38–40] Notably, besides perovskites, commonly used CTLs also degrade over time.[41,42] Regular *n-i-p* PSCs typically employ doped Spiro-MeOTAD HTLs, which, despite enabling high performance, require doping and oxidation for optimal conductivity and work function. Conventional Spiro-MeOTAD doping with Lithium *bis*(trifluoromethane)sulfonimide (LiTFSI) and 4-*tert*-butylpyridine (t-BP) involves an oxidation process lasting 10 - 24 hours, generating oxidized Spiro-MeOTAD•+TFSI⁻ radicals and ensuring uniform morphology.[43] Moreover, residual dopants and by-products (e.g., Li_xO_y) form during this process. Additionally, LiTFSI's hygroscopic nature leads to moisture absorption, converting it into *Bis*(trifluoromethanesulfonyl)amine (HTFSI), which exacerbates water uptake.[44] These factors collectively compromise the stability of the HTL and eventually lead to device failure. Additionally, FK209 is commonly utilized to enhance the conductivity of conventional Spiro-OMeTAD-based HTLs. However, it is important to note that the formation of oxidized Spiro-OMeTAD radical species typically requires substantial amounts of LiTFSI and t-BP. Literature reports indicate that approximately 56 mol% of LiTFSI and 330 mol% of t-BP are required to produce only 10 mol% of oxidized Spiro-OMeTAD radicals.[45] This high level of doping leads to the generation of undesirable by-products, highly sensitive to both moisture and thermal stress.[46] Although FK209 can slightly improve the oxidation efficiency of Spiro-OMeTAD, it still necessitates the use of high concentrations of volatile t-BP, thereby contributing further to degradation-prone by-product formation and ultimately limiting overall device stability.[47]

To address these, a recently developed ion-modulated radical-doped Spiro-MeOTAD HTL realizes optimal work function tuning through the 4-*tert*-butyl-1-methylpyridinium *bis*(trifluoromethanesulfonyl)imide (TBMPTFSI) salt modulation with improved stability.[48] Compared to the energy level optimization by chemical structure engineering of the HTL molecules, the ion-modulated radical-doped Spiro-MeOTAD HTL provides a more facile and

Open Access Article. Published on 09 January 2026. Downloaded on 1/22/2026 5:00:21 AM.
This article is licensed under a Creative Commons Attribution-NonCommercial 3.0 Unported Licence.

EES Solar Accepted Manuscript

View Article Online
DOI: 10.1039/D5EL00175G

controllable strategy to align the energy levels with reduced interfacial defects to the wide bandgap perovskites.

In this study, we have incorporated TBMPTFSI-tuned ion-modulated Spiro-MeOTAD HTLs (Ion-spiro) into the development of transparent PSCs with variable band gaps (1.52 eV, 1.61 eV, and 1.72 eV). For perovskite 2 (1.61 eV), the incorporation of Ion-Spiro results in negligible changes in photovoltaic performance, attributed to the minimal deviation of interfacial defects at the perovskite/HTL interface. In contrast, in narrow bandgap perovskites (1.52 eV), the incorporation of ion-modulated Spiro-MeOTAD with precise tuning of the TBMPTFSI doping concentration resulted in ~50 mV enhancement in the V_{OC} (1.08 V → 1.13 V). This enhancement in V_{OC} resulted in a PCE of 21.3 %, whereas the control device exhibited a maximum PCE of only 18.2 %. Similarly, perovskite 3 (1.72 eV) also showed notable improvement (~20 mV) in V_{OC} while incorporating TBMPTFSI-tuned ion-modulated Spiro-MeOTAD HTL. Optical analysis confirms that the reduction in the Shockley-Read-Hall (SRH) recombination constant achieved through Ion-Spiro incorporation suppressed interfacial defects and optimized energy level alignment, thereby enhancing the photoluminescence quantum yield (PLQY), quasi-Fermi level splitting (QFLS), and ultimately iV_{OC}. Moreover, these transparent PSCs are integrated with *n*-type tunnel oxide passivated contact (*n*-TOPCon) monocrystalline Si solar cells in a 4T tandem configuration and achieved 30.2% efficiency. Therefore, this study demonstrates that the incorporation of an ion-modulated Spiro-MeOTAD HTL provides an effective strategy for controlling interfacial defects and energy level tuning, thereby facilitating highly efficient and stable transparent PSCs for the development of Si/perovskite tandem solar cells with PCE exceeding 30%.

Results

Precise control over the band alignment between the perovskite photo-absorber and CTLs is crucial for reducing interfacial defects and consequently achieving higher photovoltage and enhanced PCE.[25] In this study, we investigate the incorporation of conventional doped Spiro-MeOTAD and ion-modulated Spiro-MeOTAD as HTLs in bandgap-varied transparent PSCs. This study comprises three different perovskites with varying A-cation and halide compositions (details attached in supporting information), which are denoted as perovskite 1 (~1.52 eV), perovskite 2 (~1.61 eV), and perovskite 3 (~1.72 eV). It is to be noted that the perovskite compositions used for this study are optimal for their respective band gaps (E_g) as per the reported literature.[49–51]

Open Access Article. Published on 09 January 2026. Downloaded on 1/22/2026 5:00:21 AM.
This article is licensed under a Creative Commons Attribution-NonCommercial 3.0 Unported Licence.

EES Solar Accepted Manuscript

View Article Online
DOI: 10.1039/D5EL00175G

Open Access Article. Published on 09 January 2026. Downloaded on 1/22/2026 5:00:21 AM.
This article is licensed under a Creative Commons Attribution-NonCommercial 3.0 Unported Licence.

EES Solar Accepted Manuscript

Figure 1 (a) illustrates the energy level alignment of perovskite materials with varying band gaps, along with control and TBMPTFSI salt-modified Ion-Spiro samples, as determined by ultraviolet photoelectron spectroscopy (UPS) in an *n-i-p* configured device architecture. With the increase in perovskite band gap, the valence band maximum (VBM) shifts gradually downward. Similarly, increasing the TBMPTFSI salt concentration in the Ion-Spiro hole-transport layer (HTL) leads to a deeper HOMO level and a downward shift of its Fermi level. These concurrent shifts in the perovskite VBM and the Ion-Spiro HOMO enable controlled tuning of the interfacial energy-level alignment. The fitted UPS spectra used for this analysis are presented in **Figure S1**. The TBMPTFSI concentration is optimized within the range of 15-20% to achieve a favourable alignment with the corresponding perovskite energy levels, as discussed in detail in subsequent sections. Additionally, conductive atomic force microscopy (C-AFM) measurements of the work function of the ion-modified Spiro-MeOTAD films exhibit good agreement with the UPS results. The corresponding variations in the contact potential difference (V_{CPD}), reflecting the work function changes, are shown in **Figure S2**. **Figure S3** compares the absorption spectra of oxidized conventional Spiro-MeOTAD with the non-oxidized ion-modulated Spiro-MeOTAD, revealing that the Ion-Spiro retains optical properties closely matching those of the oxidized counterpart.

The achievable quasi-Fermi-level splitting (QFLS) is primarily governed by the combined effects of the interfacial energy-level offset and defect states presents in control *vs.* Ion-Spiro as schematically illustrated in **Figure 1 (b)**. Notably, interfacial defect states may induce Fermi-level pinning, diminishing the impact of engineered band alignment. In such cases, the attainable QFLS becomes largely dominated by interfacial defect densities, which will be discussed in detail in the later section of this manuscript.

The stacked device architecture of the transparent PSCs employed in this study is illustrated in **Figure 1 (c)**. The architecture comprises a bilayer SnO_2 ETL, followed by perovskites with varying band gaps, and subsequently either conventional or ion-modulated Spiro-MeOTAD as the HTL. An ultra-thin WO_3 buffer layer is incorporated to mitigate sputter-induced damage, followed by an RF-deposited indium zinc oxide (IZO) layer serving as the top transparent electrode (TE), with additional silver (Ag) metal grids. The optimization of the TEs is discussed in a separate study.[52–54]

The current-voltage ($J-V$) characteristics of the bandgap-tunable transparent PSCs with both control and ion-modulated Spiro-MeOTAD HTLs are shown in **Figure 2 (a, c, and e)**. **Figure**

View Article Online
DOI: 10.1039/D5EL00175G

Open Access Article. Published on 09 January 2026. Downloaded on 1/22/2026 5:00:21 AM.
This article is licensed under a Creative Commons Attribution-NonCommercial 3.0 Unported Licence.

EES Solar Accepted Manuscript

2 (a) illustrates the $J-V$ characteristics of the transparent PSCs incorporating perovskite 1. The control device exhibits a maximum PCE of 18.2% with an V_{OC} of 1.08 V, a short-circuit current density (J_{SC}) of 25.17 mA cm^{-2}, and a fill factor (FF) of 66.9%. In contrast, the ion-modulated Spiro-MeOTAD HTL-based device demonstrates an enhancement of ~50 mV in V_{OC}, corroborating the optical analysis, resulting in a maximum V_{OC} of 1.13 V. Additionally, a slight improvement in J_{SC} and FF to 25.39 mA cm^{-2} and 73.8%, respectively, contributes to a maximum PCE of 21.3%. The external quantum efficiency (EQE) analysis, along with reflection, transmission, and integrated J_{SC} data, is displayed in **Figure 2 (b)**. Both devices exhibit a similar trend in the EQE spectrum; however, a distinct transmission spectrum is evident. Furthermore, the integrated J_{SC} values align well with the light $J-V$ analysis. **Figure 2 (c)** presents the light $J-V$ analysis of transparent PSCs incorporating perovskite 2. In contrast to perovskite 1, perovskite 2 exhibits no significant variation in V_{OC}. The control device achieves a maximum PCE of 19.1%, with V_{OC}, J_{SC}, and FF values of 1.13 V, 23.57 mA cm^{-2}, and 71.6%, respectively. Conversely, the ion-modulated Spiro-MeOTAD-based device attains a maximum PCE of 19.4%, with V_{OC}, J_{SC}, and FF values of 1.13 V, 23.70 mA cm^{-2}, and 72.5%, respectively. **Figure 2 (d)** illustrates the EQE spectrum along with transmission, reflection, and integrated J_{SC} data. Similar to perovskite 1, no significant differences are observed in the EQE and reflection spectra; however, distinct interference fringes are evident in the transmission spectrum. **Figure 2 (e)** depicts the $J-V$ analysis of transparent PSCs with perovskite 3. In corroboration with perovskite 1, a significant change in V_{OC} is noted. The control device exhibits a maximum PCE of 14.4%, with a maximum V_{OC} of 1.17 V, J_{SC} of 19.30 mA cm^{-2}, and an FF of 63.9%. In contrast, the ion-modulated Spiro-MeOTAD-based device achieves the highest PCE of 16.1%, with a maximum V_{OC} of 1.19 V, J_{SC} of 19.60 mA cm^{-2}, and an FF of 68.4%. **Figure 2 (f)** presents the EQE spectrum alongside reflection, transmission, and integrated J_{SC} data. Similar to previous studies, no significant changes in the EQE spectrum and reflection characteristics, except transmission, are observed. However, both devices exhibit distinct interference fringes, resulting in a differentiated transmission spectrum. The integrated J_{SC} values of the devices are well aligned with the light $J-V$ analysis. All the PV parameters are tabulated in **Table 1**. Furthermore, it is important to note that all $J-V$ parameters mentioned above correspond to the optimal concentration of TBMPTFSI salt. The effect of the energy level alignment and reduced interfacial defects is also evident from the built-in-potential (V_{bi}) analysis from the dark $J-V$ characteristics of the champion transparent PSCs, as shown in **Figure S4**.

View Article Online
DOI: 10.1039/D5EL00175G

Open Access Article. Published on 09 January 2026. Downloaded on 1/22/2026 5:00:21 AM.
This article is licensed under a Creative Commons Attribution-NonCommercial 3.0 Unported Licence.

EES Solar Accepted Manuscript

The optimization of ion-modulated Spiro-MeOTAD for various bandgap perovskites is performed with the tuning of TBMPTFSI salt concentration. Herein, for perovskite 1, the salt concentration is varied from 15% to 17%, and the highest V_{OC} and FF, leading to the maximum PCE, are observed at 16% doping, as shown in **Figure S5**. In addition to doping concentration, the spin-coating speed of the HTL also plays a crucial role, as the deposition process of ion-modulated Spiro-MeOTAD differs from that of conventional Spiro-MeOTAD. As the wettability and surface roughness of the perovskite surface vary with its composition, it is important to establish an optimal Ion-Spiro thickness, which in turn necessitates thickness optimization through spin-speed variation. To optimize this parameter, the spin speed is varied from 4000 rpm to 6000 rpm in increments of 1000 rpm, while maintaining the TBMPTFSI doping concentration at 16%. The results indicate that for perovskite 1, an optimal spin speed of 5000 rpm yields the highest PCE, as illustrated in **Figure S6**. Similarly, for perovskite 2, the doping concentration is varied from 16% to 19%, with the best performance observed at 17% doping, as shown in **Figure S7**. Further spin-speed optimization reveals that 3000 rpm is the most effective for perovskite 2, as depicted in **Figure S8**. Moreover, the salt concentration and film thickness were also optimized for perovskite 3. In this case, the salt concentration was varied from 18% to 20%, while the spin speed was adjusted between 3000 rpm and 5000 rpm, as shown in **Figures S9** and **S10**, respectively. It was determined that a salt concentration of 19% combined with a spin speed of 4000 rpm provided the highest PCE for perovskite 3. Notably, with increasing salt concentration, along with work function modulation, an increase in Spiro-radical concentration (SI- Experimental section) occurs, leading to enhanced conductivity, which is already reported elsewhere.[48]

The enhancement in V_{OC} likely arises from improved energy-level alignment driven by Fermi-level shifting, and/or a significant reduction in interfacial defect states. Previous studies suggest that changes in the HTL fermi level generally do not strongly affect V_{OC} because mobile ionic defects (e.g., iodine vacancy) in the perovskite, can migrate and accumulate at the perovskite/HTL interface.[55] These ions form thin Debye layers that effectively compensate for the potential differences caused by different HTM work functions. As a result, the perovskite layer self-adjusts, making V_{OC} largely insensitive to the HTL work function.

Thus, to gain a comprehensive understanding of the impact on Ion-Spiro, specifically, whether it is attributable solely to the energy level mismatch or predominantly to interfacial defects, we performed a detailed analysis of the recombination dynamics based on carrier lifetime measurements (Note 1). The fitted time-correlated single photon counting spectroscopy

View Article Online
DOI: 10.1039/D5EL00175G

Open Access Article. Published on 09 January 2026. Downloaded on 1/22/2026 5:00:21 AM.
This article is licensed under a Creative Commons Attribution-NonCommercial 3.0 Unported Licence.

EES Solar Accepted Manuscript

(TCSPC) spectra of all three perovskites with optimized salt concentration for Ion-Spiro HTL-based samples are shown in **Figure 3 (a, b, and c)**, respectively. In corroboration with $J-V$ studies, the average carrier lifetime exhibited minimal variation for perovskite 2, which is shown in **Figure 3 (b)**. The control samples of perovskite 2 showed a maximum average carrier lifetime of 34.75 ns, whereas the ion-modulated Spiro-MeOTAD samples exhibited an enhanced carrier lifetime of 53.49 ns. Moreover, there is a substantial difference in carrier lifetime observed for perovskites 1 and 3 due to a higher density of interfacial defects. Specifically, perovskite 1 exhibited carrier lifetimes of 318.79 ns and 589.76 ns for control and ion-modulated Spiro-MeOTAD samples, respectively, which is shown in **Figure 3 (a)**. Furthermore, **Figure 3 (c)** shows the TCSPC decay profile of perovskite 3, demonstrating average carrier lifetimes of 83.22 ns and 592.24 ns, respectively. It is to be noted that the significant differences in carrier lifetime across different perovskites can be attributed to bulk defects arising from variations in A-cation and halide compositions.[56–58] All the bi-exponential fitting parameters of TCSPC decay analysis are tabulated in **Table 2**. Furthermore, the TCSPC decay profiles are fitted with the equation mentioned in Note 1 (SI) to quantify recombination dynamics. The fitted parameters are tabulated in **Table 3**. The results indicate one order reduction in the SRH recombination constant (k_1) with the incorporation of Ion-Spiro HTL in all the cases.

The absorption and photoluminescence (PL) spectra of perovskites 1, 2, and 3, respectively is shown in **Figure S11**. Optical analysis confirms that, the band edge of perovskite remained unchanged with the incorporation of different HTLs, although a slight increase in the overall absorbance with ion-modulated Spiro-MeOTAD HTL incorporated sample of perovskite 1 is observed. This effect is attributed to minor degradation of the perovskite 1 with regular Spiro-MeOTAD HTL during the post-oxidation treatment. Illuminating the samples from the HTL/perovskite interface during PL analysis revealed a noticeable change in radiative intensities. Moreover, the optical analysis corroborates well with the carrier lifetime and $J-V$ analysis. Further validation of the role of interfacial defects between HTL and perovskite is performed through photoluminescence quantum yield (PLQY) analysis. The trends observed in TCSPC analyses were consistent with PLQY results. Perovskite 2 exhibited minimal PLQY differences between control and ion-modulated Spiro-MeOTAD samples, with values of 0.46% and 0.55%, respectively (**Figure 3 (b) inset**). In contrast, perovskite 1 exhibited a significant improvement from 0.28% to 1.2% upon incorporating ion-modulated Spiro-MeOTAD (**Figure 3 (a) inset**). Similarly, perovskite 3 displayed a PLQY increase from 0.31% to 3.9% (**Figure 3**

View Article Online
DOI 10.1039/D5EL00175G

Open Access Article. Published on 09 January 2026. Downloaded on 1/22/2026 5:00:21 AM.
This article is licensed under a Creative Commons Attribution-NonCommercial 3.0 Unported Licence.

EES Solar Accepted Manuscript

(c) inset). **Figure 3 (d)** illustrates the estimated quasi-Fermi level splitting (QFLS), quantified using equation (1), for all three perovskite compositions with both control and ion-modulated Spiro-MeOTAD HTLs. It is also to be noted that the observed differences in PLQY are not directly reflected in the QFLS values, which can be attributed to the logarithmic correlation between PLQY and QFLS, as described by equation (1). Further details regarding the QFLS estimation from PLQY measurements with the used parameters J_G, $J_{0,rad}$ are provided in the supporting information (SI), **Table S1** and **Figure S12,** respectively.

From the Shockley-Queisser equation of radiative recombination density of free charges (J_{rad}) with the chemical potential per free electron-hole pair, given by μ or QFLS in the active materials, can be written as,

$$J_{rad} = J_{0,rad} \cdot exp\,\frac{\mu}{k_B T} \tag{1}$$

To gain deeper insight into whether the enhancement of V_{OC} arises primarily from energy level alignment or from interfacial defects, we performed theoretical simulations for perovskite 1 by introducing band offsets between the absorber and the HTL in both the positive and negative directions, as illustrated in **Figure 4 (a)**. The simulated $J-V$ characteristics indicate that variations in band offsets do not significantly influence V_{OC}, with only minor changes observed in the FF. In contrast, simulations performed with varying k_1 reveal a clear dependence of V_{OC} on k_1, as shown in **Figure 4 (b)**. Additionally, we calculated the difference between experimentally measured and analytically determined V_{OC}, shown in **Figure 4 (c)**. The analytical values of V_{OC} are derived from the recombination constants and J_{SC}, as detailed in Note 1 (SI). The close agreement between the analytical and experimental results confirms that interfacial effects in devices employing the control Spiro-OMeTAD HTL play a dominant role in determining V_{OC}. Notably, the small variation in FF observed between the control and Ion-Spiro-based devices can be attributed primarily to differences in series resistance, as demonstrated in **Figure 4 (d)**.

Moreover, the optimized transparent PSCs with varying band gaps are coupled with a monocrystalline Si solar cell in a mechanically coupled 4T tandem configuration. **Figure 5 (a)** presents a schematic representation of the mechanically stacked 4T Si/perovskite tandem solar cells. In this configuration, *n*-type tunnel oxide passivated contact (*n*-TOPCon) Si solar cells are employed as the bottom absorbers. Sunlight is incident from the Glass/FTO side of the perovskite top cells. Short-wavelength photons were absorbed by the PSCs, while long-

View Article Online
DOI: 10.1039/D5EL00175G

wavelength photons were transmitted through the top PSCs and subsequently absorbed by the bottom Si cells. **Figure 5 (b)** illustrates the transmission spectrum of the transparent PSCs with varying band gaps, while **Figure 5 (c)** visualizes the EQE spectrum of standalone Si solar cells, along with the perovskite-filtered EQE spectrum of Si solar cells and the corresponding integrated J_{SC}. The standalone PCE of the Si solar cells is 25.5%. However, after filtering through the top PSCs, the PCE of the *n*-TOPCon Si solar cells decreased to 8.9%, 10%, and 12.3% for perovskite configurations 1, 2, and 3, respectively. The filtered efficiency of the *n*-TOPCon Si solar cells is determined based on the transmission spectrum of the individual PSCs and the EQE of the Si solar cells. The simulated integrated photocurrent density of the Si solar cells is found to be 14.67 mA cm^{-2}, 16.42 mA cm^{-2}, and 20.28 mA cm^{-2} after filtering through perovskites 1, 2, and 3, respectively. Consequently, upon adding the PCEs of the transparent PSCs with the filtered *n*-TOPCon Si solar cell performance, overall PCEs of 30.2%, 29.4%, and 28.4% are achieved for perovskite 1, 2, and 3, respectively. In all cases, the developed 4T Si/perovskite tandem solar cells are substantially more efficient than the standalone Si solar cells. Their combined efficiencies are 18.4%, 15.2%, and 11.4% higher with perovskite 1, 2, and 3, respectively. Notably, the monocrystalline *n*-TOPCon Si solar cell-based tandem configuration exhibited a substantial PCE enhancement of ~18%, increasing from 25.5% to 30.2%. The PV performance metrics of all 4T tandem solar cells are summarized in **Table 4**. **Figure 5 (d)** compares the photovoltaic performance of the 4T Si/perovskite tandem solar cells from this study with reported literature based on the active area.[59–69] The results indicate that the observed PCE is well aligned with previously reported values and represents one of the highest efficiencies among transparent PSCs when evaluated based on the active area.

The stability of transparent PSCs using both control and ion-modulated Spiro-MeOTAD are evaluated under dark N_2 storage, continuous heating at 65 °C, continuous illumination, and MPPT conditions (**Figure S13**). Across all tests, the ion-modulated Spiro-MeOTAD devices showed marginally improved stability, corroborating reduced interfacial defects and improved robustness of the organic HTL.

Discussions

This study explores the substitution of conventional LiTFSI- and t-BP-doped Spiro-MeOTAD with a post-oxidation-free, ion-modulated Spiro-MeOTAD. Along with the post-oxidation free requirement, this presented approach enables precise tuning of the work function with reduced non-radiative recombination losses at the HTL/perovskite interface through TBMPTFSI salt

Open Access Article. Published on 09 January 2026. Downloaded on 1/22/2026 5:00:21 AM.
This article is licensed under a Creative Commons Attribution-NonCommercial 3.0 Unported Licence.

EES Solar Accepted Manuscript

View Article Online
DOI: 10.1039/D5EL00175G

doping. Tuning the bandgap of perovskite absorbers *via* halide composition primarily influences the VBM, owing to the strong contribution of halide *p*-orbitals. As a result, increasing the bandgap induces a progressive downward shift (towards deeper energy levels) of the VBM, a trend also confirmed by UPS analysis.[70] Although some studies have suggested that a negative energy-band offset might hinder hole transport by creating an interfacial misalignment.[71,72] However, it is also proven that, in many cases, such conclusions likely arise from inaccuracies in determining the absolute energy levels rather than from an actual physical barrier.[71,72] Additionally, it is also well established that perovskite absorbers tend to self-adjust their interfacial energy levels, making them relatively insensitive to minor variations in the band offset with the HTL.[73]

In corroboration to that, our experimental findings, supported by theoretical modelling, indicate that the observed band offset induces only negligible variations in voltage losses and FF. Instead, the variations in the V_{OC} are predominantly governed by interfacial recombination dynamics, in agreement with the classical findings of McGehee et al., which demonstrated that the HOMO level of the HTL exerts minimal influence on the V_{OC} of PSCs.[55] These results collectively underscore that mitigating interfacial defect states, rather than optimizing energy level alignment, is critical, particularly when VBM shifts are introduced through bandgap tuning. In this context, the utilization of Ion-Spiro, a post-oxidation-free and compositionally stable HTL, represents a promising strategy for modulating the HOMO level while concurrently minimizing SRH non-radiative recombination losses. Importantly, this approach exhibits broad applicability: irrespective of whether the perovskite bandgap shifts toward higher or lower energies, Ion-Spiro facilitates the formation of a defect-suppressing and energetically favourable interface. Consequently, a pronounced reduction in interfacial recombination and an enhancement in the QFLS are achieved, as evidenced by the experimental results presented in **Figures 2**, **3**, and **4**.

Therefore, the precise tuning of HTL-induced interfacial defects with bandgap-tunable perovskites is further extended to the tandem solar cells. This study provides compelling evidence for the potential of highly efficient and stable tunable bandgap transparent PSCs for tandem applications. To evaluate this proposed strategy, three different band gaps are employed for incorporating ion-modulated Spiro-MeOTAD. It was observed that perovskite 2, with a bandgap of 1.61 eV, exhibited minimal differences in both optical and PV performance due to near-ideal interfacial defects with the regular HTLs. However, deviations from this optimal bandgap either towards narrower bandgap perovskite 1 (1.52 eV) or wider bandgap

Open Access Article. Published on 09 January 2026. Downloaded on 1/22/2026 5:00:21 AM.
This article is licensed under a Creative Commons Attribution-NonCommercial 3.0 Unported Licence.

EES Solar Accepted Manuscript

View Article Online
DOI: 10.1039/D5EL00175G

perovskite 3 (1.72 eV) resulted in significant variations in opto-electronic properties, as evidenced in **Figures 2** and **3**. Notably, upon introducing tuned TBMPTFSI-doped ion-modulated Spiro-MeOTAD, a considerable enhancement in V_{OC} and FF in perovskite 1 and 3 is observed. Further optical investigations, supported by theoretical simulations, indicate that the reduction of interfacial defects, evidenced by lower SRH recombination constants, leads to enhanced device performance. Moreover, the optimized transparent PSCs are coupled with a monocrystalline *n*-TOPCon Si solar cell with a standalone efficiency of 25.5%, yielding a maximum PCE exceeding 30%. These findings underscore the critical role of band alignment in optimizing carrier dynamics and demonstrate the effectiveness of ion-modulated Spiro-MeOTAD in mitigating interfacial defects. This is particularly significant for bandgap-varied perovskite solar cells, enabling the achievement of higher PCEs.

Conclusions

This study demonstrates the efficacy of ion-modulated Spiro-MeOTAD in replacing conventional LiTFSI- and t-BP-doped Spiro-MeOTAD HTL while eliminating post-oxidation requirements. The incorporation of TBMPTFSI salt enables a reduction in interfacial defects with tunable work function, leading to improved PV performance. The findings indicate that minimal variations in PV performance are observed for perovskite 2 (1.61 eV), as the conventional doped Spiro-MeOTAD HTL is predominantly optimized for this bandgap. However, deviations from this bandgap on either side resulted in band misalignment, increased interfacial surface defects, and reduced PCE. Notably, the introduction of ion-modulated Spiro-MeOTAD with an optimized work function significantly enhanced surface defect tolerance, thereby influencing carrier dynamics, resulting in improved 2-5% V_{OC} and 6-7% FF in perovskite 1 and 3. Thus, Ion-Spiro offers an effective strategy to enhance surface defect tolerance, irrespective of the perovskite absorber's bandgap. Moreover, the successful integration of optimized transparent PSCs with a monocrystalline *n*-TOPCon Si solar cell achieved a tandem efficiency of 30.2%, representing an ~18% improvement. These results underscore the critical role of interfacial defect passivation with ion-modulated Spiro-MeOTAD in advancing high-efficiency, stable PSCs for tandem applications, presenting a promising pathway for the next generation of photovoltaic technology.

Acknowledgements

Open Access Article. Published on 09 January 2026. Downloaded on 1/22/2026 5:00:21 AM.
This article is licensed under a Creative Commons Attribution-NonCommercial 3.0 Unported Licence.

EES Solar Accepted Manuscript

View Article Online
DOI: 10.1039/D5EL00175G

Authors are acknowledged to MoE-India for the doctoral fellowship. This work is also partially supported by the DST-Solar Challenge Award (DST/ETC/CASE/RES/2023/02). DK also acknowledged Forbes Marshall's financial support for the Energy Science & Engineering chair professorship. The authors acknowledge Rory Back and Su Verma from Pilkington for providing the FTO substrates. The authors are also thankful to MNRE sponsored NCPRE and IIT Bombay for providing all the fabrication and characterization facilities.

Open Access Article. Published on 09 January 2026. Downloaded on 1/22/2026 5:00:21 AM.
This article is licensed under a Creative Commons Attribution-NonCommercial 3.0 Unported Licence.

EES Solar Accepted Manuscript

Conflict of Interest

The authors declare no conflict of interest.

Data Availability

The experiment data can be available from the corresponding authors upon a reasonable request.

Authors Information

Abhijit Singha: Department of Energy Science and Engineering, Indian Institute of Technology Bombay, Mumbai, 400076, India; orcid.org/0000-0002-9885-1190

Tiankai Zhang: Department of Physics, Chemistry and Biology (IFM), Linköping University, Linköping, 58183, Sweden; orcid.org/0000-0001-8165-5241

Ananta Paul: Department of Metallurgical Engineering and Material Science, Indian Institute of Technology Bombay, Mumbai, 400076, India; orcid.org/0000-0003-4819-0942

M. M. Anas: Department of Electrical Engineering, Indian Institute of Technology Bombay, Mumbai, 400076, India; orcid.org/0009-0003-3569-5252

Karthik Raitani: Department of Electrical Engineering, Indian Institute of Technology Bombay, Mumbai, 400076, India; orcid.org/0000-0001-7209-4729

Manas Misra: Department of Physics, Indian Institute of Technology Bombay, Powai, Mumbai 400076, India; orcid.org/0000-0002-0023-1728

Subir Manna: Department of Physics, Indian Institute of Technology Bombay, Powai, Mumbai 400076, India; orcid.org/0009-0001-8465-4188

View Article Online
DOI: 10.1039/D5EL00175G

Vishnu Kumar: Department of Physics, Indian Institute of Technology Bombay, Powai, Mumbai 400076, India; orcid.org/0009-0006-3267-4175

Sudhanshu Mallick: Department of Metallurgical Engineering and Material Science, Indian Institute of Technology Bombay, Mumbai, 400076, India; orcid.org/0000-0002-9744-8746

K.R Balasubramaniam: Department of Energy Science and Engineering, Indian Institute of Technology Bombay, Mumbai, 400076, India; orcid.org/0000-0001-9397-5744

Pradeep R. Nair: Department of Electrical Engineering, Indian Institute of Technology Bombay, Mumbai, 400076, India; orcid.org/0000-0001-9977-2737

Feng Gao: Department of Physics, Chemistry and Biology (IFM), Linköping University, Linköping, 58183, Sweden; orcid.org/0000-0002-2582-1740

Dinesh Kabra: Department of Physics, Indian Institute of Technology Bombay, Powai, Mumbai 400076, India, orcid.org/0000-0001-5256-1465

Open Access Article. Published on 09 January 2026. Downloaded on 1/22/2026 5:00:21 AM.
This article is licensed under a Creative Commons Attribution-NonCommercial 3.0 Unported Licence.

EES Solar Accepted Manuscript

View Article Online
DOI: 10.1039/D5EL00175G

Open Access Article. Published on 09 January 2026. Downloaded on 1/22/2026 5:00:21 AM.
This article is licensed under a Creative Commons Attribution-NonCommercial 3.0 Unported Licence.

EES Solar Accepted Manuscript

References

1 J. Y. Kim, J. W. Lee, H. S. Jung, H. Shin and N. G. Park, *American Chemical Society*, 2020, preprint, DOI: 10.1021/acs.chemrev.0c00107.

2 M. A. Green and A. W. Y. Ho-Baillie, *American Chemical Society*, 2019, preprint, DOI: 10.1021/acsenergylett.9b01128.

3 O. Grånäs, D. Vinichenko and E. Kaxiras, *Sci Rep*, DOI:10.1038/srep36108.

4 M. Degani, Q. An, M. Albaladejo-Siguan, Y. J. Hofstetter, C. Cho, F. Paulus, G. Grancini and Y. Vaynzof, *Sci. Adv*, 2021, **7**, 7930.

5 S. Bitton and N. Tessler, *J Mater Chem C Mater*, 2021, **9**, 1888–1894.

6 A. Tara, A. Paul, A. Singha, S. Gohri, J. Madan, R. Pandey, P. Kumar, I. Hossain and S. Bhattarai, *Journal of Nanoparticle Research*, 2024, **26**, 278.

7 S. E. Sofia, H. Wang, A. Bruno, J. L. Cruz-Campa, T. Buonassisi and I. M. Peters, *Sustain Energy Fuels*, 2020, **4**, 852–862.

8 L. McGovern, E. C. Garnett, S. Veenstra and B. van der Zwaan, *Sustain Energy Fuels*, 2023, **7**, 5259–5270.

9 Y. Vaynzof, D. Kabra, L. Zhao, P. K. H. Ho, A. T. S. Wee and R. H. Friend, *Appl Phys Lett*, 2010, **97**, 156.

10 J. T. W. Wang, Z. Wang, S. Pathak, W. Zhang, D. W. Dequilettes, F. Wisnivesky-Rocca-Rivarola, J. Huang, P. K. Nayak, J. B. Patel, H. A. Mohd Yusof, Y. Vaynzof, R. Zhu, I. Ramirez, J. Zhang, C. Ducati, C. Grovenor, M. B. Johnston, D. S. Ginger, R. J. Nicholas and H. J. Snaith, *Energy Environ Sci*, 2016, **9**, 2892–2901.

11 G. J. A. H. Wetzelaer, M. Scheepers, A. M. Sempere, C. Momblona, J. Ávila and H. J. Bolink, *Advanced Materials*, 2015, **27**, 1837–1841.

12 T. C.-J. Yang, T. Kang, M. Fitzsimmons, G. Vega, Y. Lu, L. Rosado, A. Jiménez-Solano, L. Pan, S. J. Zelewski, J. Ferrer Orri, Y.-H. Chiang, D. Guo, Z. Y. Ooi, Y. Han, W. Xu, B. Roose, C. Ducati, S. Carretero Palacios, M. Anaya and S. D. Stranks, *EES Solar*, 2025, **1**, 41–55.

13 E. Ugur, A. A. Said, P. Dally, S. Zhang, C. E. Petoukhoff, D. Rosas-Villalva, S. Zhumagali, B. K. Yildirim, A. Razzaq, S. Sarwade, A. Yazmaciyan, D. Baran, F. Laquai, C. Deger, I. Yavuz, T. G. Allen, E. Aydin and S. De Wolf, *Science (1979)*, **385**, 533–538.

14 A. Paul, A. Singha, K. Hossain, S. Gupta, M. Misra, S. Mallick, A. H. Munshi and D. Kabra, *ACS Energy Lett*, 2024, **9**, 3019–3026.

15 S. Chozas-Barrientos, A. Paliwal, F. Ventosinos, C. Roldán-Carmona, L. Gil-Escrig, V. Held, P. Carroy, D. Muñoz and H. J. Bolink, *ACS Energy Lett*, 2025, 1733–1740.

16 S. Mariotti, E. Köhnen, F. Scheler, K. Sveinbjörnsson, L. Zimmermann, M. Piot, F. Yang, B. Li, J. Warby, A. Musiienko, D. Menzel, F. Lang, S. Keßler, I. Levine, D. Mantione, A. Al-Ashouri, M. S. Härtel, K. Xu, A. Cruz, J. Kurpiers, P. Wagner, H. Köbler, J. Li, A. Magomedov, D. Mecerreyes, E. Unger, A. Abate, M. Stolterfoht, B. Stannowski, R. Schlatmann, L. Korte and S. Albrecht, *Science (1979)*, 2023, **381**, 63–69.

View Article Online
DOI: 10.1039/D5EL00175G

Open Access Article. Published on 09 January 2026. Downloaded on 1/22/2026 5:00:21 AM.
This article is licensed under a Creative Commons Attribution-NonCommercial 3.0 Unported Licence.

EES Solar Accepted Manuscript

17 Longi, 34.6%! Record-breaker LONGi Once Again Sets a New World Efficiency for Silicon-perovskite Tandem Solar Cells.

18 D. Chojniak, M. Steiner, S. K. Reichmuth, A. Schmid, G. Siefer, S. Hooper, D. Bushnell, D. Kirk, C. Case and S. W. Glunz, *EES Solar*, 2025, **1**, 66–77.

19 Longi, 34.85%! LONGi Breaks World Record for Crystalline Silicon-Perovskite Tandem Solar Cell Efficiency Again.

20 E. Raza and Z. Ahmad, *Elsevier Ltd*, 2022, preprint, DOI: 10.1016/j.egyr.2022.04.028.

21 A. Singha, A. Paul, S. Koul, V. Sharma, S. Mallick, K. R. Balasubramaniam and D. Kabra, *Solar RRL*, DOI:10.1002/solr.202300117.

22 L. A. Zafoschnig, S. Nold and J. C. Goldschmidt, *IEEE J Photovolt*, 2020, **10**, 1632–1641.

23 S. E. Sofia, H. Wang, A. Bruno, J. L. Cruz-Campa, T. Buonassisi and I. M. Peters, *Sustain Energy Fuels*, 2020, **4**, 852–862.

24 W. Yang, H. Long, X. Sha, J. Sun, Y. Zhao, C. Guo, X. Peng, C. Shou, X. Yang, J. Sheng, Z. Yang, B. Yan and J. Ye, *Adv Funct Mater*, DOI:10.1002/adfm.202110698.

25 P. Caprioglio, J. A. Smith, R. D. J. Oliver, A. Dasgupta, S. Choudhary, M. D. Farrar, A. J. Ramadan, Y. H. Lin, M. G. Christoforo, J. M. Ball, J. Diekmann, J. Thiesbrummel, K. A. Zaininger, X. Shen, M. B. Johnston, D. Neher, M. Stolterfoht and H. J. Snaith, *Nat Commun*, DOI:10.1038/s41467-023-36141-8.

26 Q. Xue, R. Xia, C. J. Brabec and H. L. Yip, *Royal Society of Chemistry*, 2018, preprint, DOI: 10.1039/c8ee00154e.

27 C. D. Bailie, M. G. Christoforo, J. P. Mailoa, A. R. Bowring, E. L. Unger, W. H. Nguyen, J. Burschka, N. Pellet, J. Z. Lee, M. Grätzel, R. Noufi, T. Buonassisi, A. Salleo and M. D. McGehee, *Energy Environ Sci*, 2015, **8**, 956–963.

28 T. Lemercier, L. Perrin, E. Planès, S. Berson and L. Flandin, *Energies (Basel)*, DOI:10.3390/en13153794.

29 L. Lin, T. W. Jones, T. C. J. Yang, N. W. Duffy, J. Li, L. Zhao, B. Chi, X. Wang and G. J. Wilson, *Wiley-VCH Verlag*, 2021, preprint, DOI: 10.1002/adfm.202008300.

30 R. H. Ahangharnejhad, J. D. Friedl, A. B. Phillips and M. J. Heben, *Solar Energy Materials and Solar Cells*, DOI:10.1016/j.solmat.2021.111015.

31 D. Ompong and J. Singh, *Org Electron*, 2018, **63**, 104–108.

32 N. K. Kumawat, M. N. Tripathi, U. Waghmare and D. Kabra, *Journal of Physical Chemistry A*, 2016, **120**, 3917–3923.

33 L. Wang, Z. Yan, J. Qiu, J. Wu, C. Zhen, K. Tai, X. Jiang and S. Yang, *Nano Energy*, DOI:10.1016/j.nanoen.2021.106537.

34 M. Jaysankar, B. A. L. Raul, J. Bastos, C. Burgess, C. Weijtens, M. Creatore, T. Aernouts, Y. Kuang, R. Gehlhaar, A. Hadipour and J. Poortmans, *ACS Energy Lett*, 2019, **4**, 259–264.

35 Z. Zhao, W. Liu, T. Kong, Y. Liu, W. Chen, P. Gao and D. Bi, *Adv Funct Mater*, DOI:10.1002/adfm.202419393.

View Article Online
DOI: 10.1039/D3EL00175G

Open Access Article. Published on 09 January 2026. Downloaded on 1/22/2026 5:00:21 AM.
This article is licensed under a Creative Commons Attribution-NonCommercial 3.0 Unported Licence.

EES Solar Accepted Manuscript

36 Z. Wei, Q. Zhou, X. Niu, S. Liu, Z. Dong, H. Liang, J. Chen, Z. Shi, X. Wang, Z. Jia, X. Guo, R. Guo, X. Meng, Y. D. Wang, N. Li, Z. Xu, Z. Li, A. G. Aberle, X. Yin and Y. Hou, *Energy Environ Sci*, DOI:10.1039/d4ee04029e.

37 Y. Zhao, C. Wang, T. Ma, L. Zhou, Z. Wu, H. Wang, C. Chen, Z. Yu, W. Sun, A. Wang, H. Huang, B. Zou, D. Zhao and X. Li, *Energy Environ Sci*, DOI:10.1039/d2ee04087e.

38 H. Zhu, S. Teale, M. N. Lintangpradipto, S. Mahesh, B. Chen, M. D. McGehee, E. H. Sargent and O. M. Bakr, *Nature Research*, 2023, preprint, DOI: 10.1038/s41578-023-00582-w.

39 T. A. Chowdhury, M. A. Bin Zafar, M. Sajjad-Ul Islam, M. Shahinuzzaman, M. A. Islam and M. U. Khandaker, *Royal Society of Chemistry*, 2023, preprint, DOI: 10.1039/d2ra05903g.

40 A. Singha, A. Paul, N. Gaur, H. S. Bilkhu, A. Arya, V. Bhalerao, S. Mallick, K. R. Balasubramaniam and D. Kabra, *Small*, 2025, **20**, 2502659.

41 A. K. Jena, Y. Numata, M. Ikegami and T. Miyasaka, *J Mater Chem A Mater*, 2018, **6**, 2219–2230.

42 S. Y. Jeong, H. S. Kim and N. G. Park, *American Chemical Society*, 2022, preprint, DOI: 10.1021/acsami.1c21852.

43 G. Ren, W. Han, Y. Deng, W. Wu, Z. Li, J. Guo, H. Bao, C. Liu and W. Guo, *Royal Society of Chemistry*, 2021, preprint, DOI: 10.1039/d0ta11564a.

44 S. Wang, Z. Huang, X. Wang, Y. Li, M. Günther, S. Valenzuela, P. Parikh, A. Cabreros, W. Xiong and Y. S. Meng, *J Am Chem Soc*, 2018, **140**, 16720–16730.

45 S. G. Kim, T. H. Le, T. de Monfreid, F. Goubard, T. T. Bui and N. G. Park, *Advanced Materials*, DOI:10.1002/adma.202007431.

46 A. K. Jena, Y. Numata, M. Ikegami and T. Miyasaka, *J Mater Chem A Mater*, 2018, **6**, 2219–2230.

47 S. Toikkonen, G. K. Grandhi, S. Wang, B. Baydin, B. Al-Anesi, L. K. Jagadamma and P. Vivo, *Advanced Devices and Instrumentation*, DOI:10.34133/adi.0048.

48 T. Zhang, F. Wang, H.-B. Kim, I.-W. Choi, C. Wang, E. Cho, R. Konefal, Y. Puttisong, K. Terado, L. Kobera, M. Chen, M. Yang, S. Bai, B. Yang, J. Suo, S.-C. Yang, X. Liu, F. Fu, H. Yoshida, W. M. Chen, J. Brus, V. Coropceanu, A. Hagfeldt, J.-L. Brédas, M. Fahlman, D. Suk Kim, Z. Hu and F. Gao, *Science (1979)*, 2022, **377**, 495–501.

49 M. Saliba, T. Matsui, J. Y. Seo, K. Domanski, J. P. Correa-Baena, M. K. Nazeeruddin, S. M. Zakeeruddin, W. Tress, A. Abate, A. Hagfeldt and M. Grätzel, *Energy Environ Sci*, 2016, **9**, 1989–1997.

50 L. Wang, Z. Yan, J. Qiu, J. Wu, C. Zhen, K. Tai, X. Jiang and S. Yang, *Nano Energy*, DOI:10.1016/j.nanoen.2021.106537.

51 Q. Jiang, J. Tong, Y. Xian, R. A. Kerner, S. P. Dunfield, C. Xiao, R. A. Scheidt, D. Kuciauskas, X. Wang, M. P. Hautzinger, R. Tirawat, M. C. Beard, D. P. Fenning, J. J. Berry, B. W. Larson, Y. Yan and K. Zhu, *Nature*, 2022, **611**, 278–283.

52 A. Paul, A. Singha, S. Koul, S. Nayak, N. Gaur, S. Mallick, B. Kavaipatti and D. Kabra, *ACS Appl Mater Interfaces*, 2024, **16**, 60258–60267.

View Article Online
DOI: 10.1039/D5EL00175G

Open Access Article. Published on 09 January 2026. Downloaded on 1/22/2026 5:00:21 AM.
This article is licensed under a Creative Commons Attribution-NonCommercial 3.0 Unported Licence.

EES Solar Accepted Manuscript

53 A. Singha, A. Paul, S. Manna, C. K. Sahoo, V. Kumar, A. Kottantharayil, S. Mallick, K. R. Balasubramaniam and D. Kabra, *EES Solar*, DOI:10.1039/d5el00113g.

54 A. Paul, A. Singha, V. Sharma, S. Mallick, K. R. Balasubramaniam and D. Kabra, *J Phys D Appl Phys*, DOI:10.1088/1361-6463/ae00d7.

55 R. A. Belisle, P. Jain, R. Prasanna, T. Leijtens and M. D. McGehee, *ACS Energy Lett*, 2016, **1**, 556–560.

56 A. Solanki, P. Yadav, S. H. Turren-Cruz, S. S. Lim, M. Saliba and T. C. Sum, *Nano Energy*, 2019, **58**, 604–611.

57 W. Rehman, R. L. Milot, G. E. Eperon, C. Wehrenfennig, J. L. Boland, H. J. Snaith, M. B. Johnston and L. M. Herz, *Advanced Materials*, 2015, **27**, 7938–7944.

58 P. Srivastava, R. Kumar and M. Bag, *Journal of Physical Chemistry C*, 2021, **125**, 211–222.

59 Y. Zhang, L. Zhou and C. Zhang, *Multidisciplinary Digital Publishing Institute (MDPI)*, 2024, preprint, DOI: 10.3390/en17081833.

60 Y. Yao, P. Hang, B. Li, Z. Hu, C. Kan, J. Xie, Y. Wang, Y. Zhang, D. Yang and X. Yu, *Small*, DOI:10.1002/smll.202203319.

61 J. Xu, C. C. Boyd, Z. J. Yu, A. F. Palmstrom, D. J. Witter, B. W. Larson, R. M. France, J. Werner, S. P. Harvey, E. J. Wolf, W. Weigand, S. Manzoor, M. F. A M van Hest, J. J. Berry, J. M. Luther, Z. C. Holman and M. D. McGehee, *Triple-halide wide-band gap perovskites with suppressed phase segregation for efficient tandems*, 2020, vol. 367.

62 P. Löper, S. J. Moon, S. Martín De Nicolas, B. Niesen, M. Ledinsky, S. Nicolay, J. Bailat, J. H. Yum, S. De Wolf and C. Ballif, *Physical Chemistry Chemical Physics*, 2015, **17**, 1619–1629.

63 M. Schultes, T. Helder, E. Ahlswede, M. F. Aygüler, P. Jackson, S. Paetel, J. A. Schwenzer, I. M. Hossain, U. W. Paetzold and M. Powalla, *ACS Appl Energy Mater*, 2019, **2**, 7823–7831.

64 B. Chen, S. W. Baek, Y. Hou, E. Aydin, M. De Bastiani, B. Scheffel, A. Proppe, Z. Huang, M. Wei, Y. K. Wang, E. H. Jung, T. G. Allen, E. Van Kerschaver, F. P. García de Arquer, M. I. Saidaminov, S. Hoogland, S. De Wolf and E. H. Sargent, *Nat Commun*, DOI:10.1038/s41467-020-15077-3.

65 Z. Wang, X. Zhu, S. Zuo, M. Chen, C. Zhang, C. Wang, X. Ren, Z. Yang, Z. Liu, X. Xu, Q. Chang, S. Yang, F. Meng, Z. Liu, N. Yuan, J. Ding, S. Liu and D. Yang, *Adv Funct Mater*, DOI:10.1002/adfm.201908298.

66 Z. Fang, B. Deng, Y. Jin, L. Yang, L. Chen, Y. Zhong, H. Feng, Y. Yin, K. Liu, Y. Li, J. Zhang, J. Huang, Q. Zeng, H. Wang, X. Yang, J. Yang, C. Tian, L. Xie, Z. Wei and X. Xu, *Nature Communications* , DOI:10.1038/s41467-024-54925-4.

67 Z. Liu, C. Zhu, H. Luo, W. Kong, X. Luo, J. Wu, C. Ding, Y. Chen, Y. Wang, J. Wen, Y. Gao and H. Tan, *Adv Energy Mater*, DOI:10.1002/aenm.202203230.

68 L. Du, C. Li, Y. Jiang, F. Cao, C. Jia, Z. Wan, R. Meng, J. Shi, C. Xiao, Z. Liu and Z. Li, *Journal of Energy Chemistry*, 2025, **102**, 189–196.

69 Ašmontas S, Gradauskas J, Grigucevičienė A, Leinartas K, Lučun A, Mujahid M, Petrauskas K, Selskis A, Sužiedėlis A, Šilėnas A and Širmulis E, *Ukr. J. Phys. Opt. 2022*.

View Article Online
DOI: 10.1039/D5EL00175G

70 M. Wuttig, C. F. Schön, M. Schumacher, J. Robertson, P. Golub, E. Bousquet, C. Gatti and J.-Y. Raty, *Adv Funct Mater*, DOI:10.1002/adfm.202110166.

71 F. M. Rombach, S. A. Haque and T. J. Macdonald, *Royal Society of Chemistry*, 2021, preprint, DOI: 10.1039/d1ee02095a.

72 P. Schulz, D. Cahen and A. Kahn, *American Chemical Society*, 2019, preprint, DOI: 10.1021/acs.chemrev.8b00558.

73 C. Eames, J. M. Frost, P. R. F. Barnes, B. C. O'Regan, A. Walsh and M. S. Islam, *Nat Commun*, DOI:10.1038/ncomms8497.

Open Access Article. Published on 09 January 2026. Downloaded on 1/22/2026 5:00:21 AM.
This article is licensed under a Creative Commons Attribution-NonCommercial 3.0 Unported Licence.

EES Solar Accepted Manuscript

Table 1: Light $J-V$ parameters of the bandgap varying transparent PSCs with control and Ion-modulated Spiro-MeOTAD HTL

Device	HTL	Scan direction	J_{SC} (mA cm^{-2})	V_{OC} (V)	FF (%)	PCE (%)	Int. J_{SC} (mA cm^{-2})
Perovskite 1	Control	RS	25.17	1.08	66.9	18.2	24.07

View Article Online
DOI: 10.1039/D5EL00175G

		FS	24.97	1.07	62.1	16.6	
	Ion-Spiro	RS	25.39	1.13	73.8	21.3	24.22
		FS	25.31	1.10	70.7	19.7	
Perovskite 2	Control	RS	23.57	1.13	71.6	19.1	22.1
		FS	23.45	1.11	68.4	17.8	
	Ion-Spiro	RS	23.70	1.13	72.5	19.4	22.3
		FS	23.66	1.12	70.9	18.8	
Perovskite 3	Control	RS	19.30	1.17	63.9	14.4	18.3
		FS	19.36	1.13	55.9	12.2	
	Ion-Spiro	RS	19.60	1.19	68.4	16.1	18.5
		FS	18.97	1.16	64.9	14.2	

Table 2: Fitting parameters of the TCSPC carrier lifetime decay profile

Device	HTL	A1	A2	τ_1 (ns)	τ_2 (ns)	τ_{avg} (ns)
Perovskite 1	Control	0.56	0.13	39.8	431.7	318.79
	Ion- Spiro	0.41	0.34	58.3	647.5	589.76
Perovskite 2	Control	0.73	0.09	21.3	68.9	34.75
	Ion- Spiro	0.57	0.38	27.8	69.1	53.49
Perovskite 3	Control	0.53	0.34	20.1	102.7	83.22
	Ion- Spiro	0.15	0.61	39.36	601.15	592.24

Table 3: TCSPC fitting parameters of perovskite 1, 2, and 3 with control and Ion-Spiro HTL, respectively.

Sample	HTL	k_1 (S^{-1})	k_2 (cm^3S^{-1})
Perovskite 1	Control	3×10^6	5×10^{-10}

Open Access Article. Published on 09 January 2026. Downloaded on 1/22/2026 5:00:21 AM.
This article is licensed under a Creative Commons Attribution-NonCommercial 3.0 Unported Licence.

EES Solar Accepted Manuscript

View Article Online
DOI: 10.1039/D5EL00175G

	Ion-Spiro	9×10^{5}	2.5×10^{-10}
Perovskite 2	Control	1×10^{7}	2.5×10^{-10}
	Ion-Spiro	9.4×10^{6}	3×10^{-10}
Perovskite 3	Control	9×10^{6}	1×10^{-11}
	Ion-Spiro	6×10^{5}	3×10^{-11}

Table 4: 4T Si/perovskite tandem PV performance

Device	J_{SC} (mA cm^{-2})	V_{OC} (V)	FF (%)	PCE (%)
Perovskite 1	25.39	1.13	73.7	21.3
Perovskite 2	23.70	1.13	72.5	19.4
Perovskite 3	19.60	1.19	68.7	16.1
Si Stand alone	42.09	0.72	84.2	25.5
Perovskite 1-F-Si	14.67	0.72	84.2	8.9
Perovskite 2-F-Si	16.42	0.72	84.2	10
Perovskite 3-F-Si	20.28	0.72	84.2	12.3
4T (Si + Perovskite 1)	-	-	-	30.2
4T (Si + Perovskite 2)	-	-	-	29.4
4T (Si + Perovskite 3)	-	-	-	28.4

Open Access Article. Published on 09 January 2026. Downloaded on 1/22/2026 5:00:21 AM.
This article is licensed under a Creative Commons Attribution-NonCommercial 3.0 Unported Licence.

EES Solar Accepted Manuscript

View Article Online
DOI: 10.1039/D5EL00175G

Open Access Article. Published on 09 January 2026. Downloaded on 1/22/2026 5:00:21 AM.
This article is licensed under a Creative Commons Attribution-NonCommercial 3.0 Unported Licence.

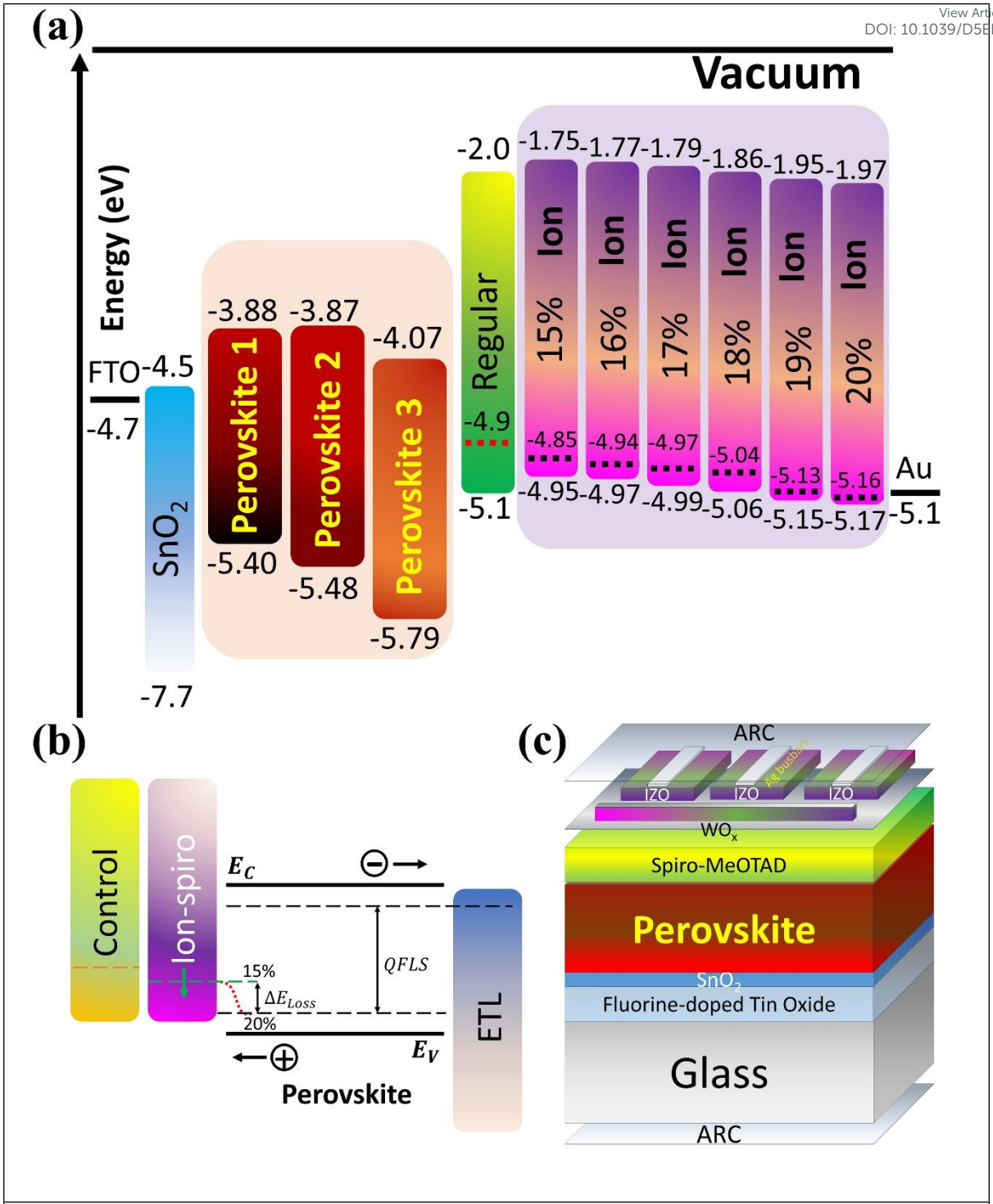

Figure 1: Role of energy level tuning with Ion-modulated Spiro-MeOTAD HTL (a) Energy level diagram of the bandgap tuneable perovskites with control and tuneable HOMO based Ion-Spiro, (b) Schematic representation of work function tuning through TBMPTFSI salt concentration for perovskites, and (c) Schematic representation of the stacked device architecture of the fabricated transparent PSCs.

EES Solar Accepted Manuscript

View Article Online
DOI: 10.1039/D5EL00175G

Open Access Article. Published on 09 January 2026. Downloaded on 1/22/2026 5:00:21 AM.
This article is licensed under a Creative Commons Attribution-NonCommercial 3.0 Unported Licence.

EES Solar Accepted Manuscript

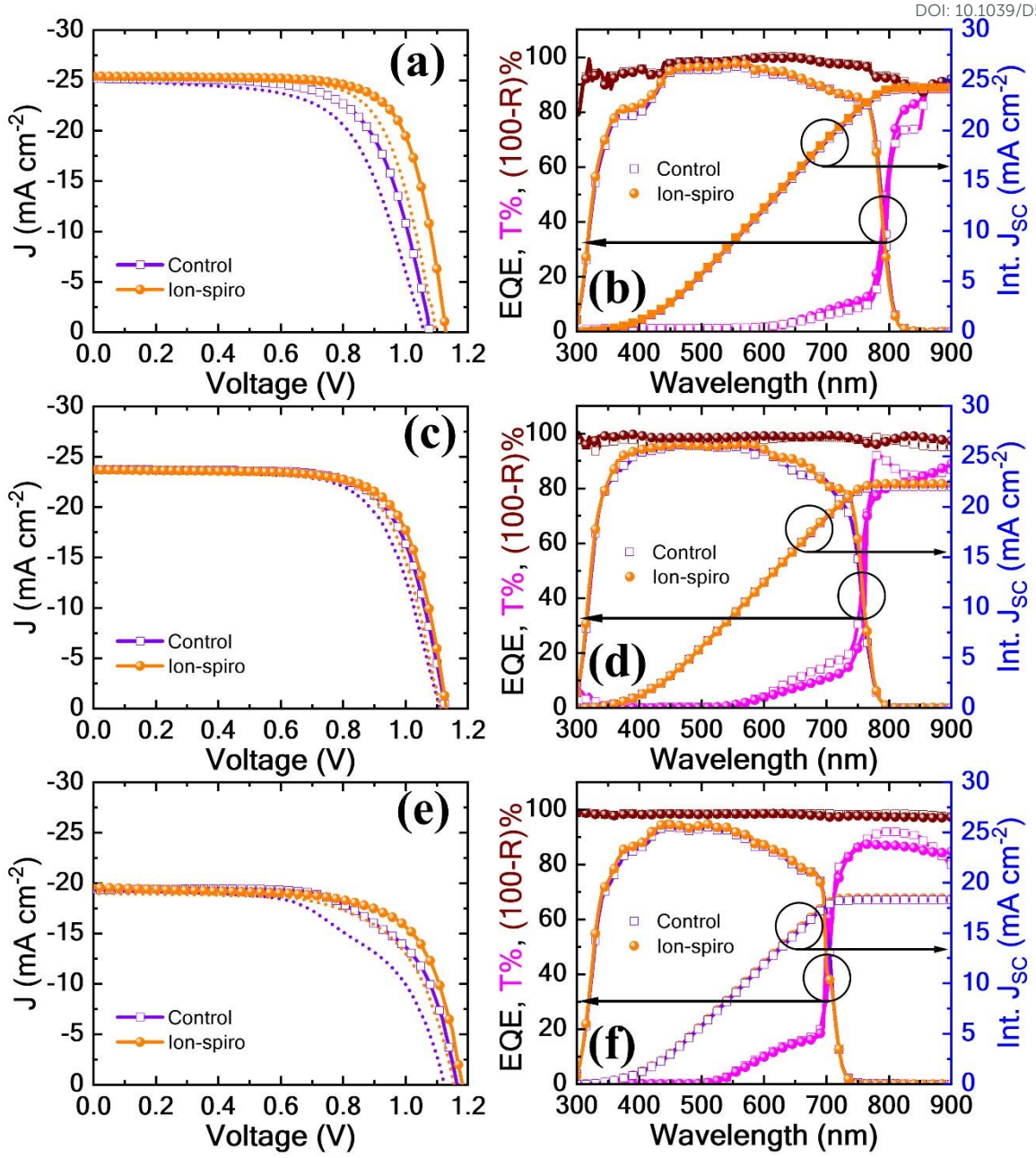

Figure 2: Photovoltaic characteristics of the bandgap varying transparent PSCs with control and Ion-modulated Spiro-MeOTAD HTL: (a, c, and e) Light $J-V$ characteristics with forward (dotted line) and reverse scan (solid line with symbol) of control (violet) and ion-spiro (orange) HTL based transparent PSCs with perovskite 1, 2, and 3, respectively. (b, d, and f) EQE with integrated J_{SC}, transmission (pink), 100-reflection (brown) of control (violet) and ion-spiro (orange) HTL-based transparent PSCs with perovskite 1, 2, and 3, respectively.

View Article Online
DOI: 10.1039/D5EL00175G

Open Access Article. Published on 09 January 2026. Downloaded on 1/22/2026 5:00:21 AM.
This article is licensed under a Creative Commons Attribution-NonCommercial 3.0 Unported Licence.

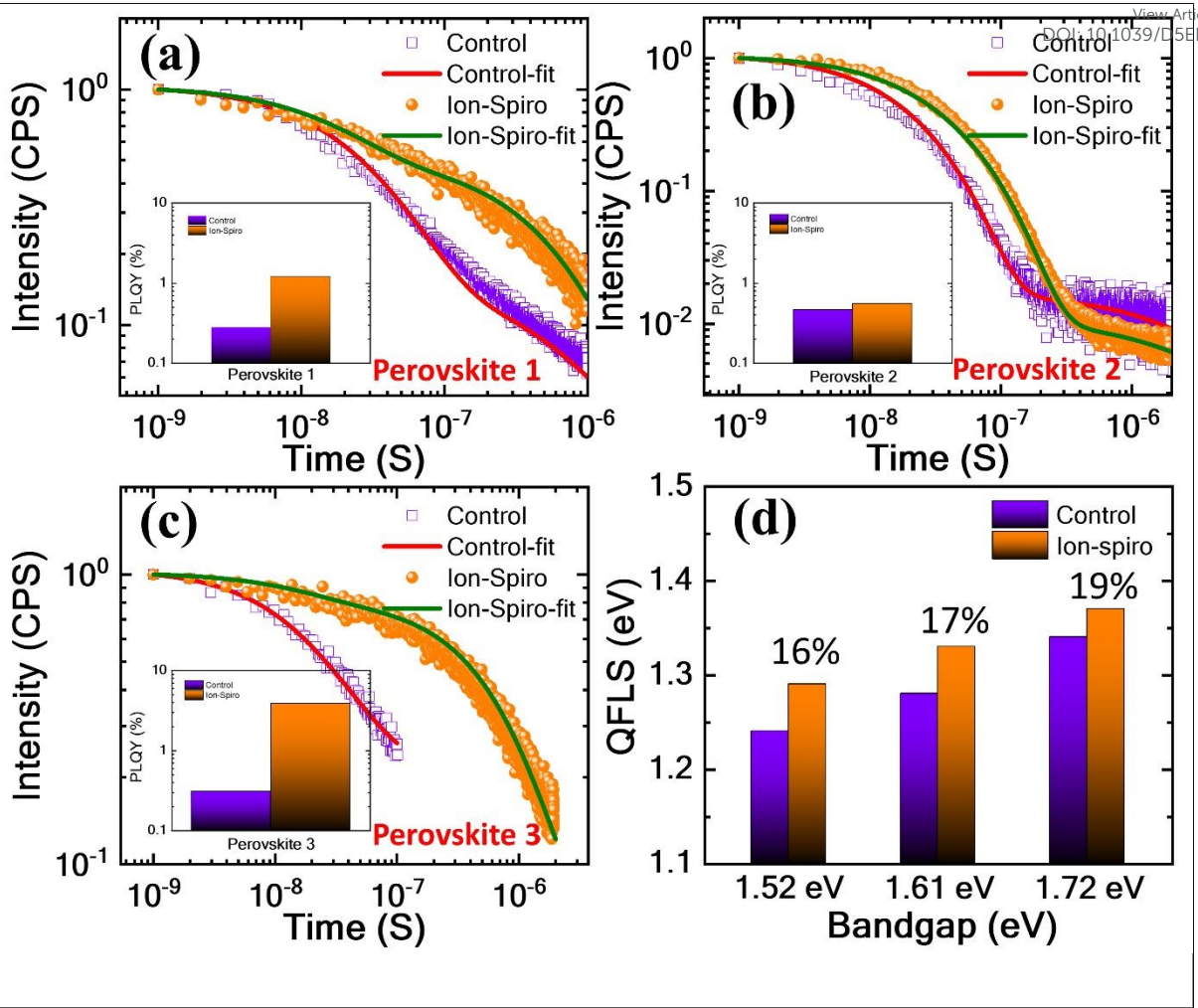

Figure 3: Optical analysis of the bandgap varying transparent semi processed PSCs (Glass/FTO/SnO_2/Perovskite/Control or ion-spiro HTL) with control and Ion-modulated Spiro-MeOTAD HTL: Fitted TCSPC carrier lifetime decay with PLQY (inset) of (a) perovskite 1, (b) perovskite 2, and (c) perovskite 3, respectively (d) estimated QFLS of bandgap varying transparent PSCs with control and Ion-modulated Spiro-MeOTAD HTL.

EES Solar Accepted Manuscript

View Article Online
DOI: 10.1039/D5EL00175G

Open Access Article. Published on 09 January 2026. Downloaded on 1/22/2026 5:00:21 AM.
This article is licensed under a Creative Commons Attribution-NonCommercial 3.0 Unported Licence.

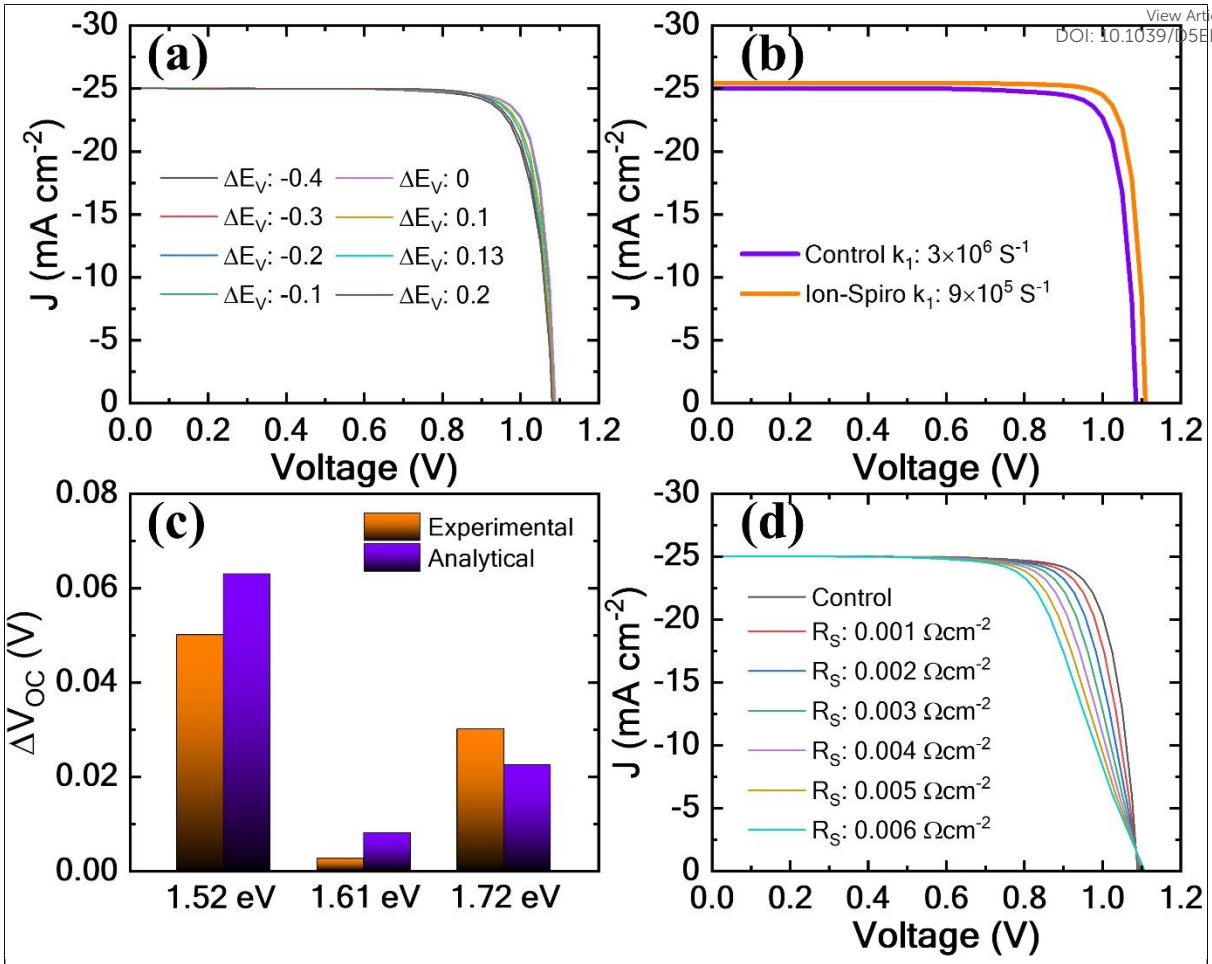

Figure 4: Theoretical validation of the role of energy-level alignment with Ion-Spiro-based devices: (a) Simulated $J-V$ characteristics of perovskite 1 under varying band offsets (both positive and negative) between the absorber and HTL, (b) effect of varying SRH recombination constant (k_1) on device performance, (c) comparison of open-circuit voltage (V_{OC}) differences between experimental measurements and analytical estimations for control and Ion-Spiro HTL-based devices, and (d) influence of varying fill factor (FF) in $J-V$ analysis under series resistance conditions.

EES Solar Accepted Manuscript

View Article Online
DOI: 10.1039/D5EL00175G

Open Access Article. Published on 09 January 2026. Downloaded on 1/22/2026 5:00:21 AM.
This article is licensed under a Creative Commons Attribution-NonCommercial 3.0 Unported Licence.

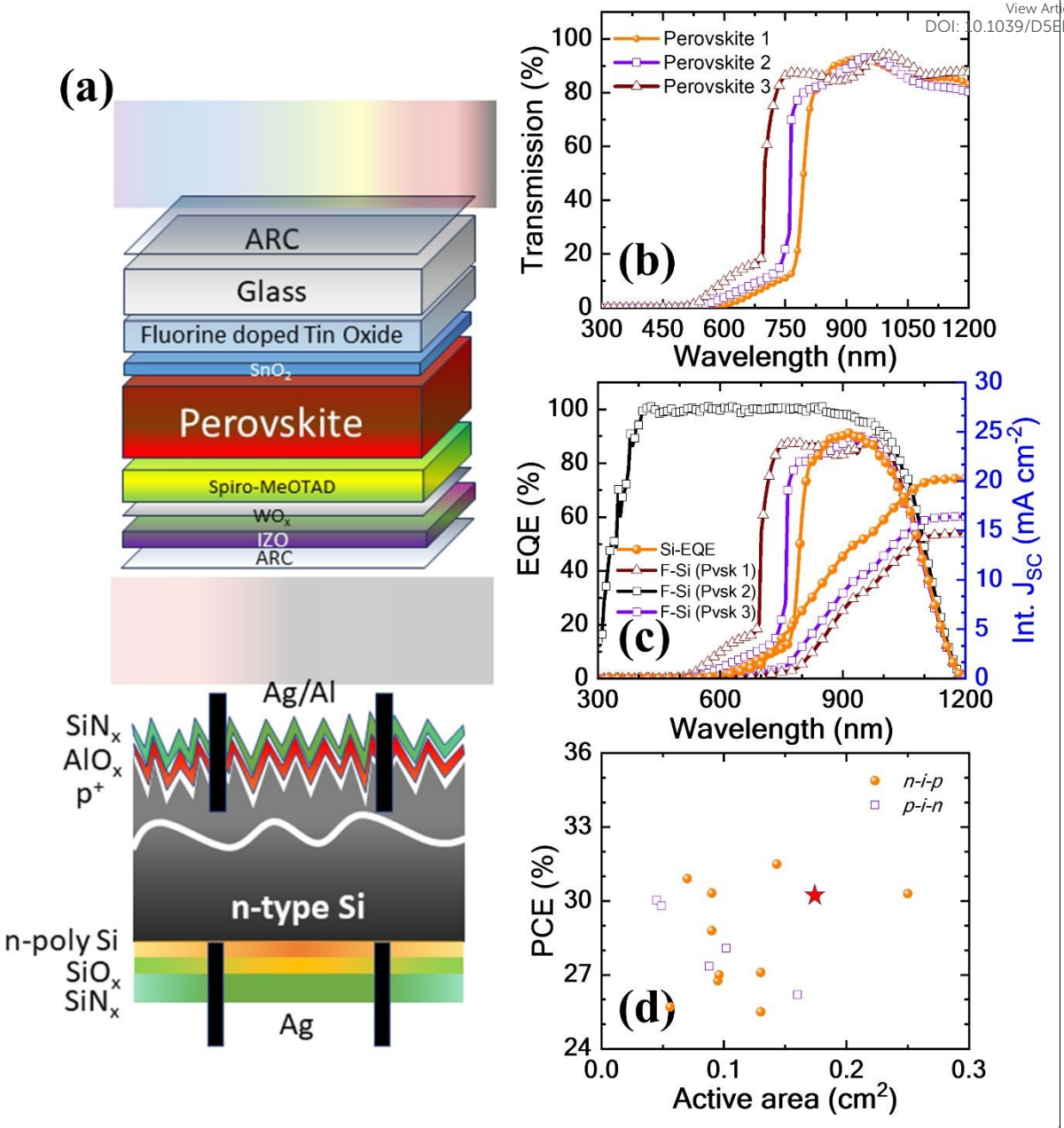

Figure 5: Mechanically stacked 4T Si/perovskite tandem solar cells: (a) Schematic representation of the device stack of mechanically coupled 4T Si/perovskite tandem solar cells, (b) transmission spectrum of the bandgap varying transparent PSCs, (c) EQE spectrum of the standalone Si and perovskite filtered Si solar cells, and (d) Comparison of the reported literature of 4T tandem efficiency with this study with respect to the active area.

EES Solar Accepted Manuscript

View Article Online
DOI: 10.1039/D5EL00175G

Data Availability

The experiment data can be available from the corresponding authors upon a reasonable request.

Open Access Article. Published on 09 January 2026. Downloaded on 1/22/2026 5:00:21 AM.
This article is licensed under a Creative Commons Attribution-NonCommercial 3.0 Unported Licence.

EES Solar Accepted Manuscript